ADVANCED FUNCTIONAL MATERIALS
www.afm-journal.de

Effective Regulation of Morphologies and Exciton-Generation Process Enables Quasi-Planar All-Polymer Organic Solar Cells Exceed 18% Efficiency

Jiaying Wang, Tianqi Chen, Wenkai Zhao, Xian Tang, Yuyang Bai, Wenying Zhou, Guankui Long, Xinyi Ji, Guanghao Lu, Wanying Feng, Xiangjian Wan, Bin Kan,* and Yongsheng Chen*

Disordered polymer chain entanglements within all-polymer blends limit the formation of optimal donor–acceptor phase separation, and thus the performance of all-polymer organic solar cells (all-PSCs). Considering the challenge and importance of morphology regulation in all-PSCs, a diluted layer-by-layer (N-LBL) strategy is thereby adopted to fine-tuning the properties of all-polymer blends. When comparing the traditional PM6:PY-IT based bulk-heterojunction (BHJ) film and PM6/PY-IT layer-by-layer (LBL) film, the N-LBL film, which is prepared from diluted PM6 (with 3% PY-IT) bottom layer and diluted PY-IT (with 6% PM6) top layer, displayed a clearer bi-continuous fibrillar network and a higher exciton generation process. Benefiting from these unique characters, the all-PSC consisting the N-LBL active layer exhibited a short-circuit current density over 26 mA cm^{-2} and a power conversion efficiency (PCE) of 18.33%, which are both higher than those of BHJ (16.88%) and LBL (17.13%) devices. Moreover, the universality of the dilution strategy in other all-polymer blends (PM6 and PY-DT, PM6 and PY-FT-*o*) is also demonstrated with unanimously improved device performance. This work underscores the effectiveness of the diluted layer-by-layer method in tuning the morphologies and charge dynamics for high-performance all-PSCs.

1. Introduction

All-polymer solar cells (all-PSCs), which leverage the unique advantages of polymer materials to achieve lightweight, flexibility, and stability device, represent a promising advancement in the field of organic solar cells (OSCs).[1] Notably, recent breakthroughs have propelled the power conversion efficiencies (PCEs) of binary all-PSCs to exceed 19%,[2] which were predominantly originated from the innovation of photovoltaic materials[3] and precise device engineering.[4] In order to obtain high-performance devices, it is vital to own an effective photovoltaic conversion process (including exciton generation, charge separation and transport, and so on) and the process is severely affected by morphology of active layer.[5] As regards to all-PSCs,[6] morphological optimization of bulk heterogeneous junction (BHJ) is considerably challenging owing to chain entanglement and the low mixing entropy between the polymer donor and acceptor, hindering the transport of charge carriers and leading more carrier recombination and charge reorganization.[7] Furthermore, the molecular stacking and orientation of long polymer chains exhibit self-aggregation and a destructive crystallization behavior, which results in excessive phase separation.[1b,8] Thus, developing a strategy to control the phase separation scale and molecular packing for all-PSCs is imperative.

Based on these challenges, the layer-by-layer (LBL) strategy is proposed as an alternative method for regulating active layer morphology.[9] This strategy can be used to manipulate and optimize the microstructure of the donor and acceptor layers, respectively. During the deposition of the top layer on the bottom layer, the swelling of the bottom layer induces inter-diffusion between various donor and acceptor, enabling the formation of a functional heterojunction framework.[10] This strategy provides an opportunity to overcome the limitations originating from the intrinsic thermodynamic properties of materials, particularly for all-polymer systems with insufficient miscibility between various acceptor.[11] Furthermore, the subsequent deposition of the donor

J. Wang, T. Chen, W. Zhao, Y. Bai, W. Zhou, G. Long, X. Ji, B. Kan
School of Materials Science and Engineering
National Institute for Advanced Materials
Nankai University
Tianjin 300350, China
E-mail: xyji06@nankai.edu.cn; kanbin04@nankai.edu.cn

X. Tang, G. Lu
Institute of Science and Technology
Xi'an Jiaotong University
Xi'an 710054, China

W. Feng, X. Wan, Y. Chen
State Key Laboratory and Institute of Elemento-Organic Chemistry
Frontiers Science Center for New Organic Matter
The Centre of Nanoscale Science and Technology and Key Laboratory of Functional Polymer Materials
Renewable Energy Conversion and Storage Center (RECAST)
College of Chemistry
Nankai University
Tianjin 300071, China

The ORCID identification number(s) for the author(s) of this article can be found under https://doi.org/10.1002/adfm.202414941

DOI: 10.1002/adfm.202414941

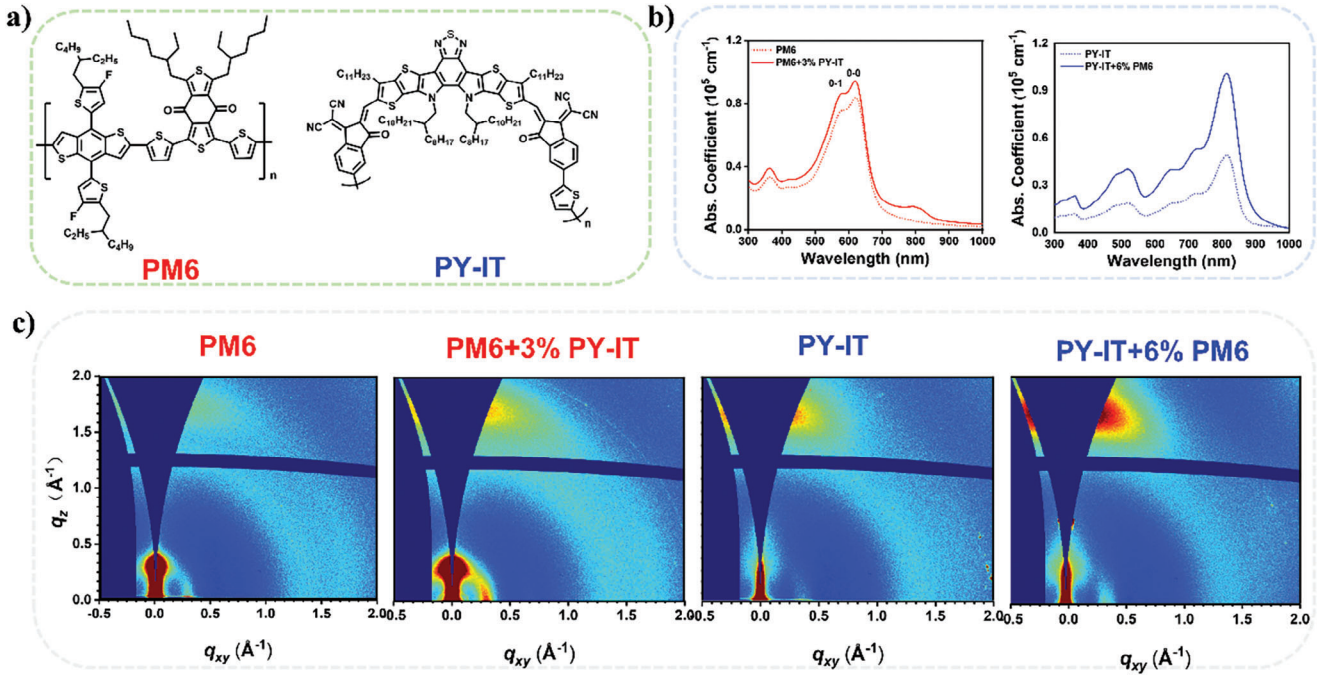

Figure 1. a) Chemical structures of PM6 and PY-IT, respectively. b) Normalized absorption profiles of PM6 and PM6+3% PY-IT, PY-IT and PY-IT+6% PM6, respectively. c) GIWAXS images of films prepared from PM6, PM6+3% PY-IT, PY-IT and PY-IT+6% PM6, respectively.

and acceptor components provides a broad processing window for fine-tuning of polymer packing and achieving more ordered molecular arrangement.[9a,12] Thus, the use of the LBL strategy to manipulate the morphology of the active layer considerably affects the enhancement of the device parameters short-circuit current densities (J_{sc}) and fill factor (*FF*).[13] Currently, based on the LBL strategy, a PCE of >18% can be achieved via the modification of the polymer donor/acceptor.[14] However, the insufficient donor/acceptor interface of the LBL structure is unbeneficial for exciton dissociation, partially due to the limited exciton diffuse distance.[15]

Much attempts have been devoted to addressing the issue of the insufficient donor/acceptor interface for the LBL-prepared devices.[16] For example, Peng et al. reported high-performance OSCs with double BHJ structure by multicomponent and LBL method. The multicomponent promotes additional photon capture and the matched material system also reduces energy loss.[16b] However, it is rather challenge to choose multicomponent of matching energy levels and compatibility between various materials. As an alternative, Bo et al. employed a diluted-LBL strategy in the material system of D18 and L8-BO, where the bottom layer is D18 with small mount L8-BO, and the top layer is L8-BO with small mount D18.[16c] This strategy not only contains sufficient BHJ's interfaces but also maintains the vertical phase distribution feature of LBL method, enabling an efficient charge transport and additionally enhancing the light absorption range. Thus, diluted-LBL strategy has great potential to make up the shortcomings for the LBL-prepared all-PSCs as discussed above.

Herein, we regulated the active layer morphology of PM6:PY-IT all-polymer blend via the dilution strategy.[17] To be specific, a small amount of PM6 was diluted into PY-IT or vice versa to form diluted donor or acceptor LBL heterojunctions. We observed that the film of PM6+3% PY-IT or PY-IT+6% PM6 displayed a higher absorption coefficient than pure film, indicating enhanced light utilization. All-PSCs were fabricated via LBL method by adopting the diluted donor (PM6+3% PY-IT) and diluted acceptor (PY-IT+6% PM6) heterojunctions, which exhibited a fast exciton generation rate (>20 $nm^3\ s^{-1}$) and an extended wavelength range of exciton generation. These conditions resulted in an excellent PCE of over 18%. The proposed strategy was also successfully applied in the fabrication of other devices, such as PY-DT and PYF-T-*o*, and achieved enhanced PCEs of 17.50% and 14.74%, respectively, compared with those of traditional BHJ structures (16.34% and 14.32%, respectively). The application of the dilution strategy to all-PSCs verified that the use of p-type semiconductor–diluted n-type semiconductor or vice versa can improve structural order and provides a new idea for the improvement of the PCE of devices.

2. Results and Discussion

2.1. Material and Properties

The chemical structures of polymer donor PM6 and polymer acceptor PY-IT are displayed in **Figure 1a**. Optimal device performance was achieved through spin-coating of PM6 with 3% PY-IT as the bottom layer and PY-IT with 6% PM6 as the top layer (optimization of the proportion of diluted ingredients is shown in the Supporting Information). To explore the effect of the dilution method on the optical properties of PM6 and PY-IT films, the UV–vis absorption spectra of the films prepared using PM6, PM6+3% PY-IT, PY-IT, and PY-IT+6% PM6 were measured. The pristine PM6 film displayed a maximum absorption peak at 621 nm, with an absorption coefficient of $0.84 \times 10^5\ cm^{-1}$

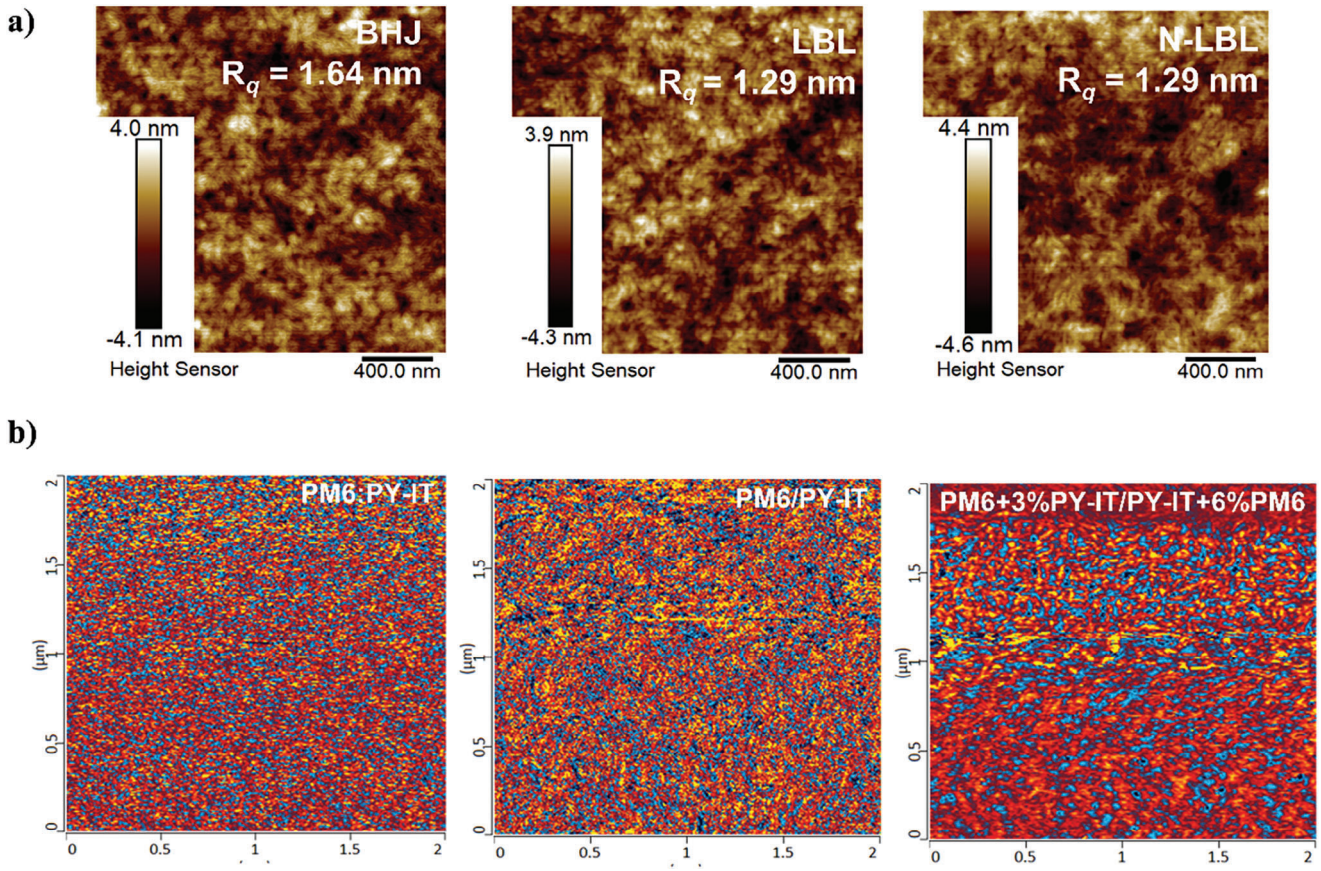

Figure 2. a) AFM height images of BHJ, LBL, N-LBL blend films, respectively. b) AFM-IR images of PM6:PY-IT, PM6/PY-IT and PM6+3% PY-IT/PY-IT+6% PM6 films.

(Figure 1b). When PM6 was diluted with 3% PY-IT (referred to as diluted PM6), the ratio of $I_{0\text{-}0}$ and $I_{0\text{-}1}$ in the two films remained similar, which indicates that the molecular stacking behaviors of PM6 in the solid state remained unaltered despite the addition of 3% PY-IT.[18] Meanwhile, compared with the pristine PM6 film, the diluted PM6 film exhibited a higher absorption coefficient of 0.94×10^5 cm^{-1}, possibly due to enhanced interactions between PM6 and PY-IT. Similarly, the dilution of PY-IT with 6% PM6 (referred to as diluted PY-IT) increased the absorption coefficient of the corresponding film, which is beneficial for improving light utilization. In comparison to the PM6:PY-IT blend film, the blend films prepared using the LBL and N-LBL methods exhibited significantly higher absorption in the acceptor-dominated region, corroborating the aforementioned results (Figure S1, Supporting Information).

Furthermore, the influence of the dilution strategy on the molecular orientation and crystallization properties was investigated using grazing-incidence wide-angle X-ray scattering (GIWAXS) characterization.[19] The GIWAXS diffraction patterns are shown in Figure 1c, with Figure S2 and Table S1 (Supporting Information) presenting the associated line-cut profiles and the corresponding parameters. Although the PM6 film and diluted PM6 film had the same π–π stacking distance ($d_{\pi-\pi}$) of 3.81 Å, the coherence length (CL) of (010) in the out-of-plane (OOP) direction increased from 24.2 Å for the PM6 film to 25.0 Å for the diluted PM6 film. This finding suggests the improved molecular crystallinity of PM6 after the addition of 3% PY-IT in the film. Furthermore, the diluted PY-IT film displayed shorter $d_{\pi-\pi}$ and CL (3.79 and 16.2 Å, respectively) than PY-IT film (3.81 and 17.2 Å). These results indicate that the addition of 6% PM6 in the PY-IT film aided in the optimization of the molecular packing motifs with shorter $d_{\pi-\pi}$ and prevented the self-aggregation of PY-IT in the film state, in agreement with the observed blue-shifted absorption profile of the diluted PY-IT film.[18] The optimized molecular packing motifs in the diluted films contributed to the enhancement of charge mobilities, as shown in Figure S3 (Supporting Information).

2.2. Morphological Investigation

Atomic force microscopy (AFM) was systematically performed to investigate the effect of the diluting strategy on the morphology of blend films. The results depicted in **Figure** 2a shows that the LBL film (refer to the film of PM6/PY-IT used layer-by-layer method) and N-LBL film (refer to the film of PM6+3% PY-IT/PY-IT+6% PM6 used diluted layer-by-layer method) exhibited smaller root-mean-square (RMS) values of 1.29 nm than the BHJ film (1.64 nm), which indicates the smoother surface of the former films. The smooth interfaces suggest more

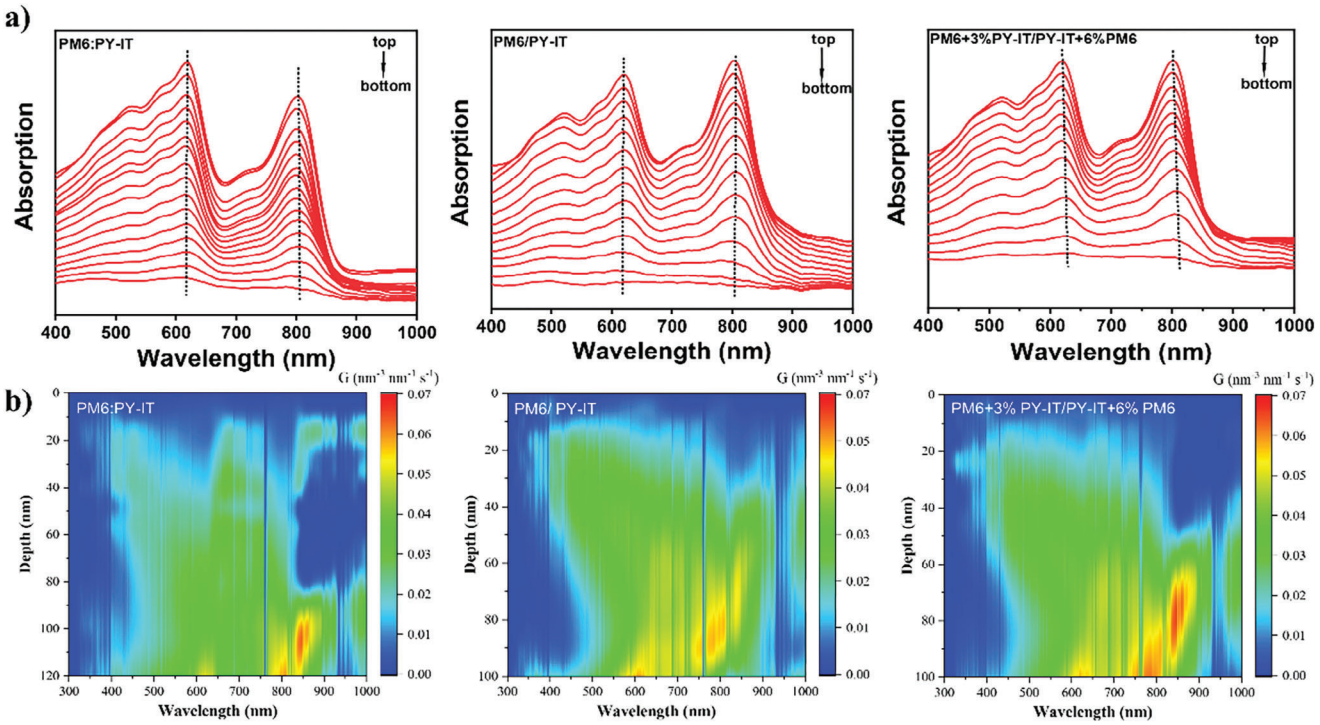

Figure 3. a) Film-depth-dependent light absorption spectra (the sub-layer thickness for each spectrum is ≈10 ± 2 nm), b) exciton generation contour as a function of film depth for BHJ, LBL, and N-LBL blend films (from left to right), where depth 0 and 100 nm represent the PNDIT-F3N/active layer and PEDOT: PSS/active layer interfaces, respectively (BHJ is 120 nm, LBL, and N-LBL are both 100 nm). For exciton generation contour, the incident light is from the ITO/ PEDOT: PSS side.

effective ohmic contact between the active layer and the top electron transporting layer, which enhanced the charge collection process in the LBL and N-LBL devices. In addition, unlike the LBL film, the N-LBL blend film exhibited clear fibril networks, which was similar to the BHJ blend film (Figure S4, Supporting Information). A long-range connective PY-IT domain was identified in the N-LBL film via AFM–infrared spectroscopy (Figure 2b), which aided in facilitating charge transport in the corresponding film.[19a]

2.3. Exciton Generation Investigation

The above preparation methods for the active layer affect its morphological features, which will impact the charge dynamic properties. Film-depth-dependent light absorption spectrometry (FLAS) quantitatively displayed the exciton generation behaviors of three blend films.[20] As displayed in **Figure 3**a, the location of the donor absorption peak remained stable from top to bottom, which indicates that PM6 maintained a uniform crystallinity at different depths and an appropriate phase separation for efficient hole transport. Conversely, in the N-LBL film, the absorption of PY-IT slightly red shifted from the top to bottom in the active layer, and this phenomenon contributed to the capture of additional photons.

A computational model of the distribution of sublayer absorption spectra was used to calculate the exciton production rate distribution. A higher number of excitons were generated in the enriched acceptor phase (over 600 nm) near the cathode region in the LBL devices compared with that in the BHJ devices (Figure 3b). Furthermore, the N-LBL device attained a higher exciton generation rate distribution than the LBL device, which indicates that the addition of 6% PY-IT to the donor phase facilitated an efficient exciton generation corresponding to the component ratio (Figure S5, Supporting Information). Most photons harvested in the PY-IT phase (750–850 nm) were converted to excitons in the bottom-half active layer (80 nm till bottom) of the BHJ and LBL devices. Notably, the N-LBL device converted the excitons obtained from the photons in the depth range of 60–100 nm at a rate of over 0.05 $nm^{-3}nm^{-1}s^{-1}$. This was accompanied by an extension of the wavelength range of exciton generation by ≈50 nm, spanning from 750 to 900 nm. The exciton generation rate profiles further revealed a peak exciton generation rate reaching 23 nm^{-3} s^{-1} (Figure S5, Supporting Information). This scenario suggests that the electrons generated from exciton dissociation may need to pass through the acceptor phase before reaching the cathode and implies that an enriched acceptor phase facilitates electron transport and collection.

2.4. Device Performance

Based on the results, conventional devices were fabricated using the all-polymer active layers of PM6 and PY-IT using BHJ, LBL, and N-LBL methods to investigate their photovoltaic performance (**Figure 4**a). The current density–voltage (*J*–*V*) curves and detailed photovoltaic parameters are shown in Figure 4b

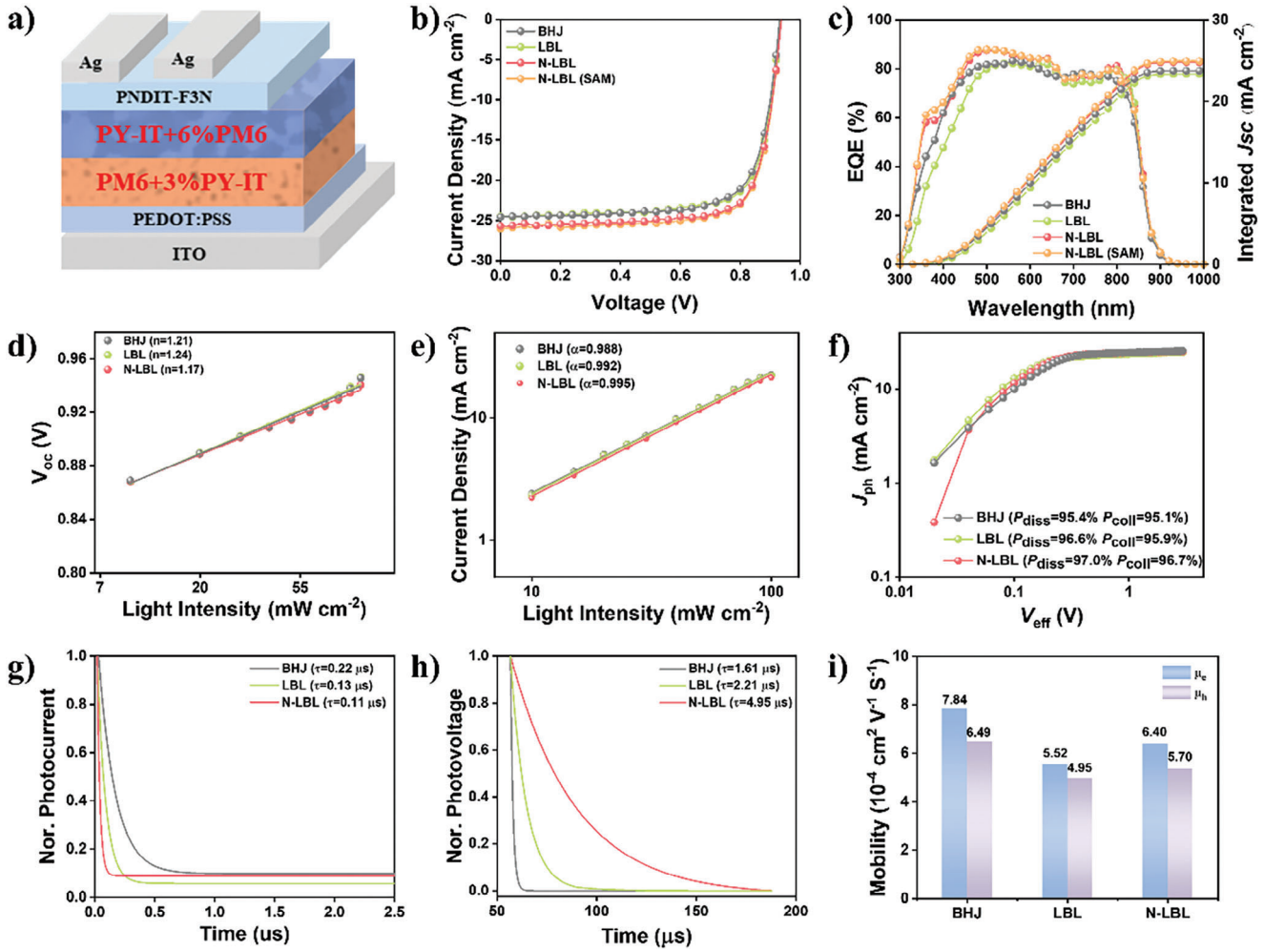

Figure 4. a) Schematic illustration of the device structure of the layer-by-layer processed all-PSCs. b) *J–V* curves of BHJ, LBL, N-LBL prepared devices. c) EQE curves and integrated J_{sc} curves of BHJ, LBL, N-LBL prepared devices. PEDOT:PSS (Heraeus Clevios P VP AI 4083) is used as the HTL, and self-assembly monolayer (SAM) Cl-2PACz is further used for N-LBL device. d) Voc versus Light Intensity. e) Current density (Jsc) versus Light Intensity. f) J_{ph} versus V_{eff}. g) Transient photocurrent (TPC) and Transient photovoltage (TPV) measurements of devices based on BHJ, LBL, N-LBL. i) Histograms of the electron mobility (μ_e) and hole mobility (μ_h).

and **Table 1**. The BHJ all-PSC achieved a PCE of 16.88%, with a V_{oc} of 0.931 V, J_{sc} of 24.57 mA cm^{-2}, and *FF* of 73.83%. The LBL all-PSC demonstrated an improved PCE of 17.13%, which mainly originated from its slightly higher *FF* of 75.00%. Encouragingly, the use of the N-LBL method resulted in an evident increment in the performance of the corresponding device with a PCE of 18.16% (Tables S2 and S3, Supporting Information). In addition to the increase in PCE, the thermal stability of N-LBL prepared device under continuous heating at 85 °C is better than that of BHJ and LBL prepared devices (Figure S6, Supporting Information). When a self-assembly monolayer (Cl-2PACz) is utilized as the hole transport layer, an excellent PCE of 18.33% was attained, accompanied by a satisfactory J_{sc} of 26.05 mA cm^{-2} and an *FF* of 75.45% for the all-PSCs. Furthermore, when D18 is used as polymer donor to form the diluted PY-IT top film, a slightly higher PCE of ≈18.5% along with a V_{OC} of 0.945 V was achieved (Table S4 and Figure S7, Supporting Information). Our study demonstrated the success of the diluted-LBL method in fabricating high-performance all-PSCs with a PCE over 18% (Table S5, Supporting Information). The improved J_{sc} of the N-LBL device not only can be ascribed to the optimized exciton generation but also to the suppressed charge recombination properties (discussed below). Furthermore, the origin of the optimized J_{sc} obtained using the N-LBL strategy was investigated through external quantum efficiency (EQE) measurement (Figure 4c). Compared with BHJ and LBL devices, the N-LBL device showed higher EQE response almost across all photoelectrical response ranges, leading to its highest integrated J_{sc} value 24.94 of mA cm^{-2}. Besides, as revealed in Figure 3a, the location of absorption peak of N-LBL device existed slight red shift from top to bottom in the PY-IT dominated region, which is beneficial for utilizing more photons and thus contributing to its higher EQE response at 750–850 nm. The integrated values (J_{cal}) obtained from the EQE curves closely matched the measured values of J_{sc}, validating the device performance derived from the *J–V* measurement.

Table 1. Photovoltaic performance parameters of all-polymer solar cells based on BHJ (PM6:PY-IT), LBL (PM6/PY-IT), and N-LBL (PM6+3% PY-IT/PY-IT+6% PM6) methods.

Devices	V_{oc} [V]	J_{sc} [mA cm^{-2}]	$J_{sc,cal}$ [mA cm^{-2}]	*FF*[%]	PCE [%]
BHJ	0.931	24.57	23.76	73.83	16.88
	(0.923 ± 0.008)	(24.38 ± 0.87)		(73.50 ± 0.33)	(16.57 ± 0.31)
LBL	0.932	24.51	23.35	75.00	17.13
	(0.930 ± 0.008)	(24.13 ± 0.76)		(74.98 ± 0.63)	(16.97 ± 0.16)
N-LBL	0.937	25.69	24.80	75.77	18.16
	(0.933 ± 0.006)	(25.39 ± 0.3)		(74.98 ± 0.8)	(17.85 ± 0.31)
	0.937	26.05	24.94	75.45	18.33[a)]
	(0.933 ± 0.004)	(25.66 ± 0.39)		(75.14 ± 0.89)	(17.97 ± 0.36)

[a)] 2Cl-2PACz is used as the hole transporting layer.

2.5. Charge Dynamic Properties

Relevant charge recombination and transport dynamics are necessary for the comprehensive understanding of device performance. Hence, the charge recombination behaviors of relevant devices were analyzed through measurement of the *J*–*V* curves under various light intensities (P_{light}).[21] The results in Figure 4d show the lower slope (n = 1.17) of the N-LBL device compared with the BHJ (n = 1.24) and LBL devices (n = 1.24), which suggests a reduced trap-assisted charge recombination in the former. Moreover, by fitting the J_{sc}-P_{light} using the equation of $J_{sc} \propto P_{in}^{\alpha}$, the α values for BHJ, LBL, and N-LBL devices reached 0.988, 0.992, and 0.995 (Figure 4e), respectively, which indicates a decreased bimolecular recombination in the N-LBL device. Charge generation and extraction were further examined through the analysis of the photocurrent density (J_{ph}) versus effective voltage (V_{eff}) under short-circuit current and maximum power output conditions (Figure 4f), respectively.[22] The calculated exciton dissociation efficiencies (η_{diss}) of the BHJ, LBL, and N-LBL devices gradually increased from 95.4% to 96.7% to 97.1%. Meanwhile, the N-LBL device achieved the most efficient charge collection properties, with the highest calculated charge collection efficiency (η_{coll}) of 96.7%. These findings indicate the excellent charge generation and collection of the N-LBL device and minimized bimolecular and trap-assisted charge recombination, which led to its superior J_{sc} values and overall device performance.

Transient photocurrent (TPC) measurements were conducted to investigate the charge dynamic properties of the above devices (Figure 4g).[23] The charge extraction time decreased in the order of BHJ (0.219 µs), LBL (0.132 µs), and N-LBL devices (0.112 µs). This finding implies that the N-LBL device exhibited less charge trapping. In addition, the photogenerated carrier lifetimes of the BHJ and LBL devices, which were determined from the transient photovoltage (TPV) measurement, reached 1.61 and 2.21 µs (Figure 4h), respectively, which are notably less than that of the N-LBL device (4.95 µs). Such findings indicate the suppressed charge carrier recombination obtained via the diluted LBL methods. In addition, the charge transport properties of the blend films were investigated using the space-charge limited current SCLC method, and the resultant *J*–*V* curves were displayed in Figure S8 (Supporting Information). The BHJ device demonstrated high electron/hole mobilities of $7.84 \times 10^{-4}/6.49 \times 10^{-4}$ cm^2 V^{-1} S^{-1} with a μ_e/μ_h of 1.20, and the LBL device showed relatively lower values of $5.52 \times 10^{-4}/4.95 \times 10^{-4}$ cm^2 V^{-1} S^{-1} with a μ_e/μ_h of 1.11. On the other hand, the N-LBL device achieved improved electron/hole mobilities of $6.40 \times 10^{-4}/5.57 \times 10^{-4}$ cm^2 V^{-1} S^{-1} compared with those of the LBL device (Figure 4i; Table S6, Supporting Information). The relatively high and balanced charge transport in the N-LBL device was conducive to swift charge extraction and reduced charge accumulation, which accounted for its high J_{sc} and improved photovoltaic performance.

2.6. Molecular Dynamics (MD) Simulation

MD simulations were performed to investigate the application of the BHJ, LBL, and N-LBL methods on the microstructures of molecular packing and vertical separation of all-polymer donors and acceptors. **Figure 5a** shows that the LBL and N-LBL films exhibited a higher heterogeneity than the BHJ film. To illustrate the molecular packing scenarios, the radial distribution functions (RDFs) between the donor and the acceptor were calculated (Figures S9 and S10, Supporting Information). Eight distinct packing conditions were identified, with the combination of FE (the repeating unit of BDD in PM6 defined as E and the signal thiophene in PY-IT defined as F) playing a crucial role in π–π packing. All conditions demonstrated substantial increases in the range of 3.8–4.0 Å, which corresponded to the π–π packing distances determined through GIWAX analysis. Furthermore, the π–π packing peaks (3.8–4.0 Å) observed for the RDFs varied considerably among the various systems, with the BHJ system exhibiting the highest peak with the N-LBL system. The LBL system displayed the lowest peak, which corresponded to its less dense molecular packing. Although the N-LBL system had a lower stacking density than the BHJ system, it achieved enhanced device performance through the strategic reduction of the number of stacks to improve the vertical phase separation. This optimized vertical phase separation helped to improve the interfaces between molecules, enhancing the effectiveness of charge transport.

For more detailed analyses of the amorphous forms investigated in the present work, a more detailed analysis was conducted through characterization of the dimer configurations arising from two adjacent molecules. This characterization was based on two key parameters: the distance between the centers of mass

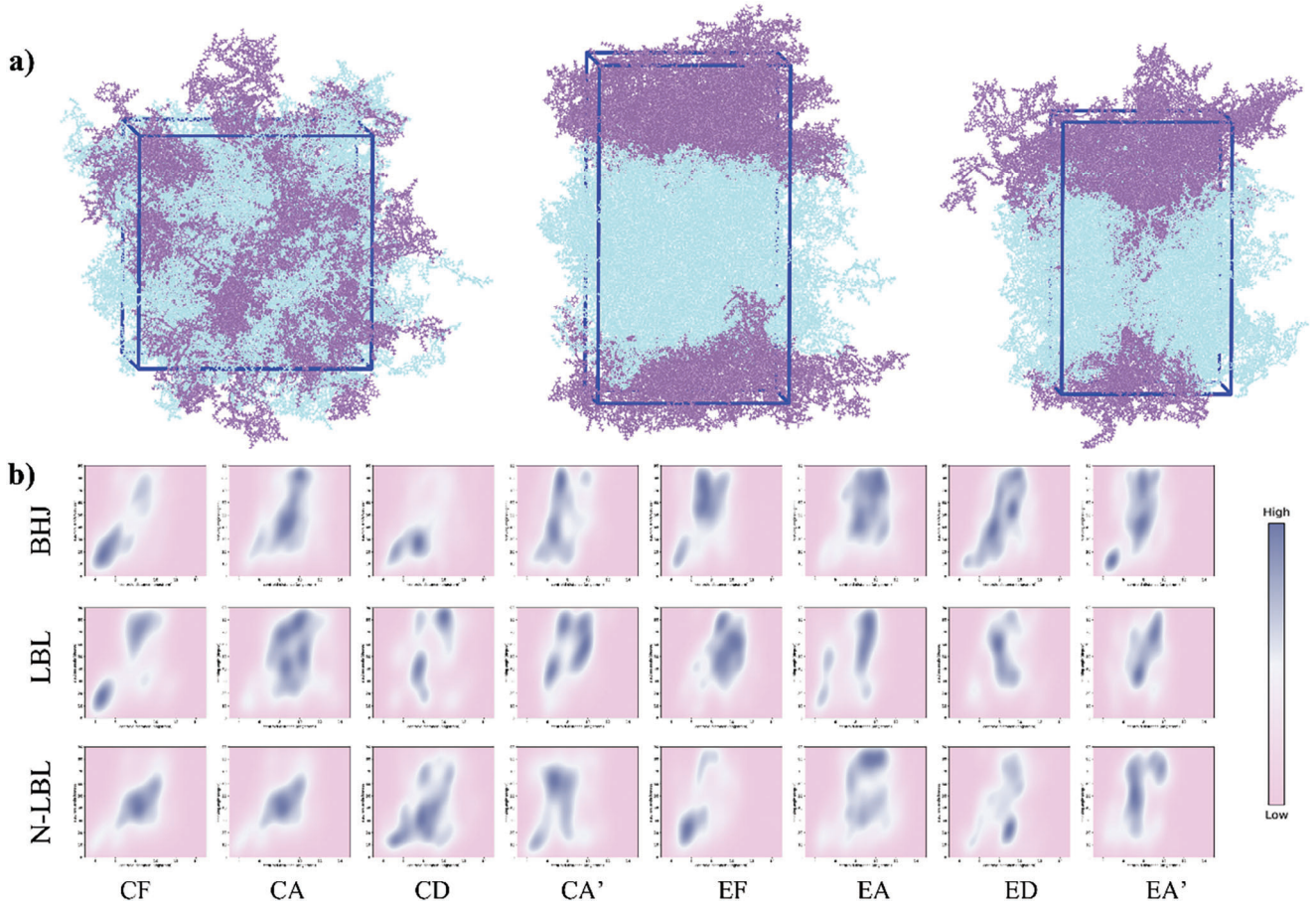

Figure 5. a) MD simulation of the structure of BHJ, LBL, and N-LBL, where the Powder Blue and Soft Purple colors correspond to PM6 and PY-IT, respectively. b) Density heatmaps of d (COM distance) – φ (dihedral angle between two molecular planes) of molecular pairs in the final MD boxes. The two molecules with the shortest atomic distance between the atoms of two parts smaller than 0.5 nm are defined as a pair. Abscissa represents the centroid distance. The Ordinate is stacking angle. When smaller centroid distance, deeper stacking angle, two parts means that formed the excellent stacking degree.

(COM) of the molecular backbones (d) and the dihedral angle (φ) between the planes of two molecules. The density heatmaps of d–φ can be found in Figure 4b. An arrangement was classified as a face-on orientation at the dihedral angle φ less than 30° and COM distance d less than 0.8 nm. This type of orientation promoted the most robust parallel π–π stacking interactions, which resulted in an enhanced electronic coupling indicative of an improved charge transfer rate. Across most packing conditions, the BHJ system displayed a higher density regarding face-on configurations. Contrastingly, in specific packing conditions, such as CD (the repeating unit of FBDT in PM6 is defined as C and the donor-strong electron group in NFA defined as D) and CA' (central acceptor unit defined as A'), the N-LBL system demonstrated the superior density of face-on configurations. Particularly, BHJ systems exhibited a total stacking count of 240.30 per unit volume (Table S7, Supporting Information). The counts were 47.31 and 89.44 for the N-LBL and LBL configurations, respectively. When focusing solely on face-on stacking, the numbers were 45.83 for BHJ, 5.99 for N-LBL, and 16.18 for LBL films, respectively (Table S8, Supporting Information). Thus, the total and face-on stacking counts followed the trend BHJ > N-LBL > LBL. In general, a high stacking count improves electronic interactions, such as charge transfer. The trends of the total and face-on stacking counts corresponded to the heights of π–π packing peaks observed for the RDFs, which highlight the effectiveness of the strategy employed in the N-LBL systems. Through a reduced stacking density, the N-LBL improved the vertical phase separation, which in turn optimized molecular orientation and distribution. As a result, an improved PCE was observed in the devices.

2.7. Universality of N-LBL Strategy

All the findings demonstrate the effectiveness of the diluted-LBL method in improving charge generation and balancing charge transport behaviors in all-polymer blends. In addition, this approach can be used to optimize an active layer morphology with an improved film crystallinity compared with the traditional LBL method. In addition, the universality of this strategy was confirmed using two other polymer acceptors, PY-DT and PYF-T-*o*. The *J*–*V* curves of PY-DT- and PYF-T-*o*-based devices were obtained (Figure S11, Supporting Information), with device

parameters summarized in Table S9 (Supporting Information). Compared with the BHJ devices, the devices using the N-LBL method showed improvements in J_{sc} and *FF* while maintaining the original V_{oc}. As a result, higher PCEs of 17.50% and 14.74% were obtained for the PM6:PY-DT and PM6:PY-FT-*o* devices, respectively. Compared with those of as-cast devices, the N-LBL device displayed higher EQE responses, which indicates a more efficient photoelectrical conversion processes with an improved J_{sc}. Overall, these results are consistent with those for PM6:PY-IT-based devices and underscore the effectiveness of the N-LBL method in attaining high-performance all-PSCs.

3. Conclusion

In summary, the diluted-LBL strategy was adopted to fabricate high-performance all-PSCs with optimized active layer morphology. This strategy presented increased D/A interpenetrating regions and compressed molecule packing, which promotes exciton generation and dissociation and facilitates charge transport with improved carrier dynamics. The N-LBL (PM6+3% PY-IT/PY-IT+6% PM6) device achieved an impressive PCE of 18.33% along with increased V_{oc} of 0.937 V, J_{sc} of 26.05 mA cm^{-2}, and *FF* of 75.45%, surpassing that of conventional BHJ (16.88%) and LBL (17.13%) devices. It is highlighted that we ascribed the improvement in PCE to enhance exciton utilization efficiency, for that more photons were captured in rich acceptor phase that generates amounts of excitons in active layer from 750 to 900 nm. Moreover, this diluted structure exhibited universality in the enhancement of the performance of various all-polymer OSCs, for example, from 16.34% of BHJ to 17.50% of N-LBL for PM6:PY-DT, from 14.32% of BHJ to 16.34% of N-LBL for PM6:PY-FT-*o*, respectively. The diluted-LBL strategy not only approves the importance of innovative active layer structures in tuning morphologies but also provides a new pathway for improving the device performance of all-PSCs.

Supporting Information

Supporting Information is available from the Wiley Online Library or from the author.

Acknowledgements

The authors gratefully acknowledge the financial support from Ministry of Science and Technology of the People's Republic of China (2022YFB4200400, 2019YFA0705900, 2023YFE0210400), National Natural Science Foundation of China (52303237, 21935007, 52025033, and 22361132530), and the Fundamental Research Funds for the Central Universities, Nankai University (023-632343116). The authors thank Dr. Yu Chen at Beijing Synchrotron Radiation Facility, Institute of High Energy Physics for performing GIWAXS measurements.

Conflict of Interest

The authors declare no conflict of interest.

Data Availability Statement

The data that support the findings of this study are available from the corresponding author upon reasonable request.

Keywords

all-polymer, exciton-generation, morphology, organic solar cells, quasi-planar heterojunction

Received: August 15, 2024
Revised: September 10, 2024
Published online:

[1] a) J. Hou, O. Inganäs, R. H. Friend, F. Gao, *Nat. Mater.* **2018**, *17*, 119; b) G. Wang, F. S. Melkonyan, A. Facchetti, T. J. Marks, *Angew. Chem., Int. Ed.* **2019**, *58*, 4129; c) C. Duan, L. Ding, *Sci. Bull.* **2020**, *65*, 1508; d) H. Sun, X. Guo, A. Facchetti, *Chem* **2020**, *6*, 1310.

[2] a) R. Sun, T. Wang, Q. Fan, M. Wu, X. Yang, X. Wu, Y. Yu, X. Xia, F. Cui, J. Wan, *Joule* **2023**, *7*, 221; b) W. Feng, T. Chen, Y. Li, T. Duan, X. Jiang, C. Zhong, Y. Zhang, J. Yu, G. Lu, X. Wan, *Angew. Chem.* **2024**, *136*, 202316698; c) W. Xu, H. Tian, Y. Ni, Y. Xu, L. Zhang, F. Zhang, S. Wu, S. Y. Jeong, T. Huang, X. Du, *Chem. Eng. J.* **2024**, *493*, 152558; d) G. Zhang, C. Zhao, L. Zhu, L. Wang, W. Xiong, H. Hu, Q. Bai, Y. Wang, C. Xie, P. You, *Energy. Environ. Mater.* **2023**, *7*, e12683; e) Z. Wang, X. Wang, L. Tu, H. Wang, M. Du, T. Dai, Q. Guo, Y. Shi, E. Zhou, *Angew. Chem.* **2024**, *136*, 202319755; f) R. Jiang, M. Nilam, A. Hennig, W. M. Nau, *Adv. Mater.* **2024**, *36*, 2306922; g) L. Tu, H. Wang, W. Duan, R. Ma, T. Jia, T. A. D. Peña, Y. Luo, J. Wu, M. Li, X. Xia, *Energy. Environ. Sci.* **2024**, *17*, 3365.

[3] a) X. Li, X. Kong, G. Sun, Y. Li, *eScience* **2023**, 100171; b) Y.-J. Hwang, N. M. Murari, S. A. Jenekhe, *Polym. Chem.* **2013**, *4*, 3187; c) H. Zhuo, X. Li, J. Zhang, C. Zhu, H. He, K. Ding, J. Li, L. Meng, H. Ade, Y. Li, *Nat. Commun.* **2023**, *14*, 7996; d) S. Li, W. Liu, C. Z. Li, M. Shi, H. Chen, *Small* **2017**, *13*, 1701120; e) A. K. Hundal, S. Ali, M. Jameel, L. Jones, N. Kaur, R. A. Evans, J.-L. Li, S. J. Langford, A. Gupta, *Mater. Chem. Front.* **2020**, *4*, 3209; f) Z. G. Zhang, Y. Yang, J. Yao, L. Xue, S. Chen, X. Li, W. Morrison, C. Yang, Y. Li, *Angew. Chem.* **2017**, *129*, 13688; g) Z. G. Zhang, Y. Li, *Angew. Chem., Int. Ed.* **2021**, *60*, 4422.

[4] a) S. Luo, C. Li, J. Zhang, X. Zou, H. Zhao, K. Ding, H. Huang, J. Song, J. Yi, H. Yu, *Nat. Commun.* **2023**, *14*, 6964; b) Z. Li, F. Peng, X. Qian, J. Li, Z. Zhong, L. Ying, H. Wu, F. Huang, Y. Cao, *J. Mater. Chem. C* **2022**, *10*, 6710; c) K. Hu, C. Zhu, K. Ding, S. Qin, W. Lai, J. Du, J. Zhang, Z. Wei, X. Li, Z. Zhang, *Energy. Environ. Sci.* **2022**, *15*, 4157; d) J. Ge, L. Hong, W. Song, L. Xie, J. Zhang, Z. Chen, K. Yu, R. Peng, X. Zhang, Z. Ge, *Adv. Energy. Mater.* **2021**, *11*, 2100800; e) S. Li, Z. Li, X. Wan, Y. Chen, *eScience* **2023**, *3*, 100085; f) J. Jing, Y. Dou, S. Chen, K. Zhang, F. Huang, *eScience* **2023**, *3*, 100142.

[5] a) G. Yu, J. Gao, J. C. Hummelen, F. Wudl, A. J. Heeger, *Science* **1995**, *270*, 1789; b) W. Ma, C. Yang, X. Gong, K. Lee, A. J. Heeger, *Adv. Funct. Mater.* **2005**, *15*, 1617; c) Y. Xie, F. Yang, Y. Li, M. A. Uddin, P. Bi, B. Fan, Y. Cai, X. Hao, H. Y. Woo, W. Li, *Adv. Mater.* **2018**, *30*, 1803045; d) K. Weng, L. Ye, L. Zhu, J. Xu, J. Zhou, X. Feng, G. Lu, S. Tan, F. Liu, Y. Sun, *Nat. Commun.* **2020**, *11*, 2855.

[6] X. Ouyang, R. Peng, L. Ai, X. Zhang, Z. Ge, *Nat. Photonics.* **2015**, *9*, 520.

[7] a) J. W. Lee, C. Sun, B. S. Ma, H. J. Kim, C. Wang, J. M. Ryu, C. Lim, T. S. Kim, Y. H. Kim, S. K. Kwon, *Adv. Energy. Mater.* **2021**, *11*, 2003367; b) B. Liu, H. Sun, J.-W. Lee, J. Yang, J. Wang, Y. Li, B. Li, M. Xu, Q. Liao, W. Zhang, *Energy. Environ. Sci.* **2021**, *14*, 4499; c) L. Zhu, M. Zhang, W. Zhong, S. Leng, G. Zhou, Y. Zou, X. Su, H. Ding, P. Gu, F. Liu, *Energy. Environ. Sci.* **2021**, *14*, 4341.

[8] a) R. Zeng, L. Zhu, M. Zhang, W. Zhong, G. Zhou, J. Zhuang, T. Hao, Z. Zhou, L. Zhou, N. Hartmann, *Nat. Commun.* **2023**, *14*, 4148; b) M. Deng, X. Xu, W. Qiu, Y. Duan, R. Li, L. Yu, Q. Peng, *Angew. Chem.* **2024**, *63*, 202405243; c) S. Ma, B. Li, S. Gong, J. Wang, B. Liu, S. Y.

Jeong, X. Chen, H. Y. Woo, K. Feng, X. Guo, *Angew. Chem., Int. Ed.* **2023**, *62*, 202308306.

[9] a) L. Zhan, S. Li, X. Xia, Y. Li, X. Lu, L. Zuo, M. Shi, H. Chen, *Adv. Mater.* **2021**, *33*, 2007231; b) Y. Sun, L. Nian, Y. Kan, Y. Ren, Z. Chen, L. Zhu, M. Zhang, H. Yin, H. Xu, J. Li, *Joule* **2022**, *6*, 2835; c) X. Wu, Y. Wu, S. Peng, L. Xiao, Z. Xiao, W. Zhang, G. Ren, Y. Min, Y. Liu, *Sol. RRL* **2023**, *7*, 2300136; d) C. Zhao, R. Ma, J. Oh, L. Wang, G. Zhang, Y. Wang, S. He, L. Zhu, C. Yang, G. Zhang, *J. Mater. Chem. C* **2022**, *10*, 17899; e) W. Xu, X. Zhu, X. Ma, H. Zhou, X. Li, S. Y. Jeong, H. Y. Woo, Z. Zhou, Q. Sun, F. Zhang, *J. Mater. Chem. A* **2022**, *10*, 13492; f) Y. Zhang, B. Wu, Y. He, W. Deng, J. Li, J. Li, N. Qiao, Y. Xing, X. Yuan, N. Li, *Nano. Energy.* **2022**, *93*, 106858.

[10] a) Y. Dou, L. Hong, J. Jing, T. Jia, J. Zhang, K. Zhang, F. Huang, *Sol. RRL* **2023**, *7*, 2300599; b) H. Ning, Q. Jiang, P. Han, M. Lin, G. Zhang, J. Chen, H. Chen, S. Zeng, J. Gao, J. Liu, *Energy. Environ. Sci.* **2021**, *14*, 5919; c) J. Qin, Q. Yang, J. Oh, S. Chen, G. O. Odunmbaku, N. A. N. Ouedraogo, C. Yang, K. Sun, S. Lu, *Adv. Sci.* **2022**, *9*, 2105347.

[11] a) J. C. Aguirre, S. A. Hawks, A. S. Ferreira, P. Yee, S. Subramaniyan, S. A. Jenekhe, S. H. Tolbert, B. J. Schwartz, *Adv. Energy. Mater.* **2015**, *5*, 1402020; b) M. Li, Q. Wang, J. Liu, Y. Geng, L. Ye, *Mater. Chem. Front.* **2021**, *5*, 4851; c) H. Hu, M. Ghasemi, Z. Peng, J. Zhang, J. J. Rech, W. You, H. Yan, H. Ade, *Adv. Mater.* **2020**, *32*, 2005348.

[12] a) D. Li, C. Guo, X. Zhang, B. Du, P. Wang, S. Cheng, J. Cai, H. Wang, D. Liu, H. Yao, *Aggregate* **2022**, *3*, e72; b) X. Xu, L. Yu, H. Meng, L. Dai, H. Yan, R. Li, Q. Peng, *Adv. Funct. Mater.* **2022**, *32*, 2108797; c) Q. Wu, W. Wang, Y. Wu, Z. Chen, J. Guo, R. Sun, J. Guo, Y. Yang, J. Min, *Adv. Funct. Mater.* **2021**, *31*, 2010411; d) P. Cheng, R. Wang, J. Zhu, W. Huang, S. Y. Chang, L. Meng, P. Sun, H. W. Cheng, M. Qin, C. Zhu, *Adv. Mater.* **2018**, *30*, 1705243; e) H. Fu, W. Gao, Y. Li, F. Lin, X. Wu, J. H. Son, J. Luo, H. Y. Woo, Z. Zhu, A. K. Y. Jen, *Small. Methods.* **2020**, *4*, 2000687.

[13] a) R. Sun, Q. Wu, J. Guo, T. Wang, Y. Wu, B. Qiu, Z. Luo, W. Yang, Z. Hu, J. Guo, *Joule* **2020**, *4*, 407; b) H. Tian, W. Xu, Z. Liu, Y. Xie, W. Zhang, Y. Xu, S. Y. Jeong, F. Zhang, N. Weng, Z. Zhang, *Adv. Funct. Mater.* **2024**, *34*, 2313751.

[14] L. Wang, C. Chen, Z. Gan, C. Liu, C. Guo, W. Xia, W. Sun, J. Cheng, Y. Sun, J. Zhou, *J. Energy. Chem* **2024**, *96*, 345.

[15] a) L. Zhang, M. Zhang, Y. Ni, W. Xu, H. Zhou, S. Ke, H. Tian, S. Y. Jeong, H. Y. Woo, W.-Y. Wong, *ACS Mater. Lett.* **2024**, *6*, 2964; b) W. Xu, M. Zhang, X. Ma, X. Zhu, S. Y. Jeong, H. Y. Woo, J. Zhang, W. Du, J. Wang, X. Liu, *Adv. Funct. Mater.* **2023**, *33*, 2215204; c) H. Tian, Y. Ni, W. Zhang, Y. Xu, B. Zheng, S. Y. Jeong, S. Wu, Z. Ma, X. Du, X. Hao, *Energy. Environ. Sci.* **2024**, *17*, 5173.

[16] a) L. Wen, H. Mao, L. Zhang, J. Zhang, Z. Qin, L. Tan, Y. Chen, *Adv. Mater.* **2024**, *36*, 2308159; b) X. Xu, W. Jing, H. Meng, Y. Guo, L. Yu, R. Li, Q. Peng, *Adv. Mater.* **2023**, *35*, 2208997; c) H. Zhang, Y. Liu, G. Ran, H. Li, W. Zhang, P. Cheng, Z. Bo, *Adv. Mater.* **2024**, *36*, 2400521; d) L. Wang, C. Chen, Y. Fu, C. Guo, D. Li, J. Cheng, W. Sun, Z. Gan, Y. Sun, B. Zhou, *Nat. Energy.* **2024**, *9*, 208.

[17] a) J. Yuan, Y. Zhang, L. Zhou, G. Zhang, H.-L. Yip, T.-K. Lau, X. Lu, C. Zhu, H. Peng, P. A. Johnson, *Joule* **2019**, *3*, 1140; b) Z. Luo, T. Liu, R. Ma, Y. Xiao, L. Zhan, G. Zhang, H. Sun, F. Ni, G. Chai, J. Wang, *Adv. Mater.* **2020**, *32*, 2005942.

[18] J. Song, Y. Li, Y. Cai, R. Zhang, S. Wang, J. Xin, L. Han, D. Wei, W. Ma, F. Gao, Y. Sun, *Matter* **2022**, *5*, 4047.

[19] a) X. Gu, Y. Wei, N. Yu, J. Qiao, Z. Han, Q. Lin, X. Han, J. Gao, C. Li, J. Zhang, X. Hao, Z. Wei, Z. Tang, Y. Cai, X. Zhang, H. Huang, *CCS Chem.* **2023**, *5*, 2576; b) H. Chen, Y. Zou, H. Liang, T. He, X. Xu, Y. Zhang, Z. Ma, J. Wang, M. Zhang, Q. Li, *Sci China. Chem.* **2022**, *65*, 1362.

[20] a) H. Fu, Z. Peng, Q. Fan, F. R. Lin, F. Qi, Y. Ran, Z. Wu, B. Fan, K. Jiang, H. Y. Woo, G. Lu, H. Ade, A. K.-Y. Jen, *Adv. Mater.* **2022**, *34*, 2202608; b) J. Yu, Z. Shen, W. Lu, Y. Zhu, Y.-X. Liu, D. Neher, N. Koch, G. Lu, *Adv. Funct. Mater.* **2023**, *33*, 2302089; c) L. Bu, M. Hu, W. Lu, Z. Wang, G. Lu, *Adv. Mater.* **2018**, *30*, 1704695.

[21] J.-W. Lee, C. Sun, C. Lee, Z. Tan, T. N.-L. Phan, H. Jeon, D. Jeong, S.-K. Kwon, Y.-H. Kim, B. J. Kim, *ACS Energy. Lett.* **2023**, *8*, 1344.

[22] F. Qi, Y. Li, R. Zhang, F. R. Lin, K. Liu, Q. Fan, A. K. Y. Jen, *Angew. Chem.* **2023**, *135*, 202303066.

[23] H. Yu, Y. Wang, H. K. Kim, X. Wu, Y. Li, Z. Yao, M. Pan, X. Zou, J. Zhang, S. Chen, *Adv. Mater.* **2022**, *34*, 2200361.